Editors' Suggestion

Photocurrents induced by structured light

A. A. Gunyaga, M. V. Durnev, and S. A. Tarasenko
Ioffe Institute, 194021 St. Petersburg, Russia

(Received 4 July 2023; revised 17 August 2023; accepted 18 August 2023; published 5 September 2023)

Advances in manipulating the structure of optical beams enable the study of interaction between structured light and low-dimensional semiconductor systems. We explore the photocurrents in two-dimensional systems excited by such inhomogeneous radiation with structured electromagnetic field. Besides the contribution associated with the intensity gradient, the photocurrent contains contributions driven by the gradients of the Stokes polarization parameters and the phase of the electromagnetic field. We develop a microscopic theory of the nonlinear, nonlocal intraband transport of electrons induced by electromagnetic field of structured radiation and derive analytical expressions for the photocurrent contributions. The theory is applied to analyze the radial and azimuthal photocurrents excited by twisted radiation beams carrying orbital angular momentum, and possible experiments to detect the photocurrents are discussed.

DOI: 10.1103/PhysRevB.108.115402

I. INTRODUCTION

Structured light, extending from intensity or polarization gratings to beams carrying orbital angular momentum and fields with fully controlled spatiotemporal structure, has a variety of applications in spectroscopy, metrology, quantum information processing, etc. [1–4]. While significant progress has been achieved recently in the optical methods of structuring the light beams [5–8] and controlling the optical forces acting on micro- and nanoscale dielectric particles [9–14], less is known so far about the interaction of structured light beams with charge carriers in low-dimensional semiconductor systems. The latter research area, bridging advances in optics and solid-state physics [15–18], is intriguing from a fundamental point of view and crucial for the development of optoelectronics.

The electron-photon interaction in semiconductors is sensitive to the local field polarization and the local symmetry breaking [19,20]. This underlies the physics of photogalvanic effects, where the ac electric field of linearly or circularly polarized radiation drives dc electric currents in noncentrosymmetric structures [21–30]. The key feature of structured light is that the electromagnetic field parameters, such as polarization or phase, vary at the scale of light wavelength. This length is typically much larger than the scale of nonlocality in semiconductors, which makes it challenging to study the photoresponse associated with the light structure. Nevertheless, several groups have recently reported the observation of the photocurrents induced by the Laguerre-Gaussian beams and sensitive to the orbital angular momentum of light [15–17]. These advances open a new page in the research of photoelectric phenomena in solids and stimulate theoretical studies of the photocurrents induced by structured light. Theoretical results in the field are limited so far to the phenomenological analysis of the photocurrents [15,17], numerical quantum-mechanical calculations of nonstationary currents in quantum rings and dots [31–33], and the quantum-mechanical calculation of the rotational photon drag [34]. The latter belongs to the family of photon drag effects being extensively studied in different material systems and geometries [35–48].

Here, we develop a microscopic theory of photocurrents induced in two-dimensional electron systems by structured radiation. We explore what types of direct currents can be driven by spatially inhomogeneous electromagnetic waves acting upon free carriers. It is found that, besides the contribution associated with the intensity gradient, the photocurrent contains contributions driven by the gradients of the Stokes polarization parameters and the phase of the electromagnetic field. In particular, the photocurrent emerging between the domains excited by left-handed and right-handed circularly polarized radiation can be interpreted as the chiral edge current between the photoinduced topological phases with the opposite Floquet-Chern numbers [49,50]. In the framework of Boltzmann kinetic theory, we derive analytical expressions for all the photocurrent contributions corresponding to the intraband transport of electrons.

The developed theory is applied then to analyze the spatial distribution of the photocurrents induced by twisted-light beams; see Fig. 1. In this geometry, the emergent photocurrent $\boldsymbol{j}(\boldsymbol{r})$ has both radial and azimuthal components which are controlled by the parameters of the beam. The radial photocurrents lead to a redistribution of electric charge in the two-dimensional plane and form the radial photovoltage. The azimuthal photocurrents induce a static magnetic field and the corresponding magnetization. We calculate the photovoltage and the static magnetic field and discuss their dependence on the beam angular momentum and polarization.

II. KINETIC THEORY

We consider a two-dimensional electron gas (2DEG) in the xy plane (at $z = 0$) which is irradiated by a spatially inhomogeneous monochromatic electromagnetic wave. In the 2DEG plane, the electric field has the form

$$\boldsymbol{E}(\boldsymbol{r}, t) = \boldsymbol{E}(\boldsymbol{r})e^{-i\omega t} + \text{c.c.}, \tag{1}$$

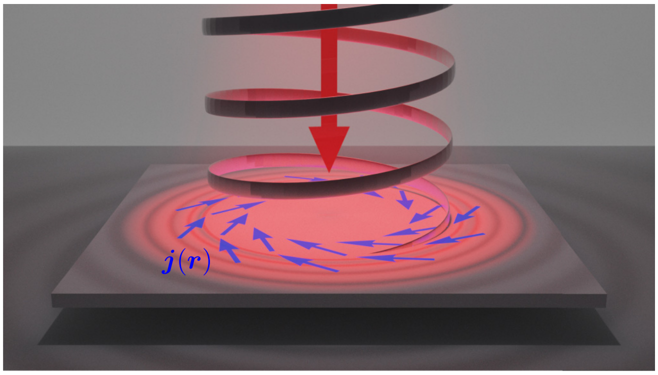

FIG. 1. Photocurrents induced by structured light. Inhomogeneous ac electric field of twisted radiation beam generates dc electric current $\boldsymbol{j}(r)$ in two-dimensional electron gas.

where $\boldsymbol{E}(\boldsymbol{r})$ is the field amplitude and $\boldsymbol{r} = (x, y)$ is the in-plane coordinate. Generally, because of screening, the spatial profile of the electric field acting upon the electrons differs from that of the incident wave. The total field can be calculated in the framework of the Lindhard screening theory [51,52]. However, for the amplitude $\boldsymbol{E}(\boldsymbol{r})$ which varies smoothly in the 2DEG plane, i.e., in the long-wavelength limit, screening is negligible. This regime reliably holds for electromagnetic fields of radio-frequency and terahertz spectral ranges with the inhomogeneity scale of the order of the wavelength [53]. Therefore, we neglect the difference between the profiles of the incident and actual electric fields.

The electromagnetic field necessarily contains the magnetic component $\boldsymbol{B}(\boldsymbol{r}, t) = \boldsymbol{B}(\boldsymbol{r})e^{-i\omega t} + \text{c.c.}$ with the out-of-plane projection

$$B_z = -i\frac{c}{\omega}\left(\frac{\partial E_y}{\partial x} - \frac{\partial E_x}{\partial y}\right), \tag{2}$$

which follows from the Maxwell equation. In the model of 2D transport, the electrons interact only with the in-plane component $\boldsymbol{E}_\parallel = (E_x, E_y)$ of the electric field and the out-of-plane component B_z of the magnetic field.

The electron kinetics in the presence of electric and magnetic fields is described by the Boltzmann equation

$$\frac{\partial f}{\partial t} + \boldsymbol{v}\cdot\boldsymbol{\nabla} f + e\left[\boldsymbol{E}_\parallel(\boldsymbol{r}, t) + \frac{1}{c}\boldsymbol{v}\times\boldsymbol{B}(\boldsymbol{r}, t)\right]\cdot\frac{\partial f}{\partial \boldsymbol{p}} = I\{f\}, \tag{3}$$

where $f(\boldsymbol{p}, \boldsymbol{r}, t)$ is the electron distribution function, $\boldsymbol{p} = (p_x, p_y)$ and $\boldsymbol{v} = \boldsymbol{p}/m^*$ are the momentum and velocity, respectively, $\boldsymbol{\nabla} = \partial/\partial\boldsymbol{r}$ is the 2D nabla operator, e is electron charge, m^* is the effective mass, and $I\{f\}$ is the collision integral. In what follows, we do calculations in the relaxation time approximation and take the collision integral in the form

$$I\{f\} = -\frac{f - \langle f\rangle}{\tau}, \tag{4}$$

where $\langle f\rangle$ is the distribution function averaged over the directions of $\boldsymbol{p}$, and τ is the relaxation time.

The dc electric currents emerge in the second order in the ac field amplitude. Therefore, we solve Eq. (3) iteratively by expanding the distribution function $f(\boldsymbol{p}, \boldsymbol{r}, t)$ in the series in the field amplitude as follows,

$$f(\boldsymbol{p}, \boldsymbol{r}, t) = f_0 + [f_1(\boldsymbol{p}, \boldsymbol{r})e^{-i\omega t} + \text{c.c.}] + f_2(\boldsymbol{p}, \boldsymbol{r}), \tag{5}$$

where $f_0(\varepsilon)$ is the equilibrium distribution function, $\varepsilon = p^2/2m^*$ is the electron energy, $f_1 \propto E$ is the first-order correction, and f_2 is the stationary second-order correction which determines the dc current. The correction f_2 contains contributions $\propto EE^*$ and $\propto EB^*, BE^*$. Other second-order corrections, such as $\propto EE$ and $\propto EB$, oscillate at 2ω and do not contribute to the dc current.

The functions f_1 and f_2 satisfy the differential equations, which follow from Eq. (3),

$$-i\omega f_1 + \boldsymbol{v}\cdot\boldsymbol{\nabla} f_1 + e\boldsymbol{E}_\parallel(\boldsymbol{r})\cdot\frac{\partial f_0}{\partial\boldsymbol{p}} = I\{f_1\}, \tag{6}$$

$$\boldsymbol{v}\cdot\boldsymbol{\nabla} f_2 + \left\{e\left[\boldsymbol{E}_\parallel(\boldsymbol{r}) + \frac{1}{c}\boldsymbol{v}\times\boldsymbol{B}(\boldsymbol{r})\right]\cdot\frac{\partial f_1^*}{\partial\boldsymbol{p}} + \text{c.c.}\right\} = I\{f_2\}\,. \tag{7}$$

The term with the Lorentz force in Eq. (6) vanishes because $\partial f_0/\partial\boldsymbol{p} \propto \boldsymbol{p}$ and $\boldsymbol{v}\times\boldsymbol{B}$ is orthogonal to $\boldsymbol{p}$.

The local density of the dc electric current is given by

$$\boldsymbol{j}(\boldsymbol{r}) = e\nu\sum_{\boldsymbol{p}}\boldsymbol{v} f_2(\boldsymbol{p}, \boldsymbol{r}), \tag{8}$$

where ν is the factor of spin/valley degeneracy. Multiplying Eq. (7) by $\boldsymbol{v}$, summing up the result over $\boldsymbol{p}$, and integrating the term $\propto \partial f_1^*/\partial\boldsymbol{p}$ by parts, one obtains

$$\begin{aligned}\boldsymbol{j}(\boldsymbol{r}) = &-e\nu\tau\sum_{\boldsymbol{p}}\boldsymbol{v}(\boldsymbol{v}\cdot\boldsymbol{\nabla} f_2) + \frac{e^2\nu\tau}{m^*}\left[\boldsymbol{E}_\parallel(\boldsymbol{r})\sum_{\boldsymbol{p}} f_1^* + \text{c.c.}\right]\\ &-\frac{e^2\nu\tau}{m^* c}\left[\boldsymbol{B}(\boldsymbol{r})\times\sum_{\boldsymbol{p}}\boldsymbol{v} f_1^* + \text{c.c.}\right].\end{aligned} \tag{9}$$

To proceed further we take into account that the field is smoothly varying in the 2DEG plane; i.e., the scale of the field variation L is much larger than the mean free path of electrons $l = v_F\tau$ and v_F/ω, where v_F is the Fermi velocity. Assuming that $L \gtrsim \lambda$, where $\lambda = 2\pi c/\omega$ is the wavelength of the incident field, the above conditions reduce to $l \ll \lambda$ and $v_F \ll c$. The former inequality holds very well for radio-frequency and terahertz fields even in high-mobility systems (1 THz corresponds to $\lambda \sim 0.3$ mm). The latter inequality is automatically fulfilled for conduction-band electrons in solids. We also note that the electric field screening by 2DEG is negligible if $L \gg (2\pi\sigma/c)\lambda$, where σ is the 2D conductivity. This condition can be readily fulfilled, particularly in the paraxial approximation of the incident radiation. However, the effects of screening can play an important role if $L \ll \lambda$, which can be achieved, e.g., in plasmonic structures where the electric field is enhanced near small metal particles located at the 2DEG plane.

For smoothly varying fields, the gradients of the field components and the distribution function are small and can be treated perturbatively. We do such calculations for the photocurrent Eq. (9) in the first order of l/L.

The third term in Eq. (9) contains $B_z(\boldsymbol{r})$, which is already determined by the field gradients [see Eq. (2)]; therefore, the sum $\sum_{\boldsymbol{p}}\boldsymbol{v} f_1^*$ can be calculated in the local response approximation. Multiplying Eq. (6) by $\boldsymbol{v}$, summing up the resulting equation over $\boldsymbol{p}$, and neglecting the gradient term $\propto \nabla f_1$ one obtains

$$\sum_{\boldsymbol{p}} \boldsymbol{v} f_1 = \frac{\sigma}{e\nu} \boldsymbol{E}_\parallel(\boldsymbol{r}), \tag{10}$$

where σ is the conductivity,

$$\sigma = \frac{ne^2\tau}{m^*(1 - i\omega\tau)}, \tag{11}$$

and $n = \nu \sum_{\boldsymbol{p}} f_0$ is the 2D electron density.

The sum $\sum_{\boldsymbol{p}} f_1^*$ in the second term in Eq. (9) can be calculated by summing up Eq. (6) over $\boldsymbol{p}$ and using Eq. (10), which gives

$$\sum_{\boldsymbol{p}} f_1 = -\frac{i\sigma}{e\nu\omega} \nabla \cdot \boldsymbol{E}_\parallel(\boldsymbol{r}), \tag{12}$$

where $\nabla \cdot \boldsymbol{E}_\parallel = \partial E_x/\partial x + \partial E_y/\partial y$.

The first term in Eq. (9) is determined by the gradient of f_2; therefore the sums $\sum_{\boldsymbol{p}} v_\alpha v_\beta f_2$ can be also calculated in the local response approximation. The function f_2 contains the zero and second angular harmonics which both contribute to the sums $\sum_{\boldsymbol{p}} v_\alpha v_\beta f_2$ since

$$\sum_{\boldsymbol{p}} v_\alpha v_\beta f_2 = \sum_{\boldsymbol{p}} \frac{v^2}{2} \delta_{\alpha\beta} f_2 + \sum_{\boldsymbol{p}} \left(v_\alpha v_\beta - \frac{v^2}{2} \delta_{\alpha\beta} \right) f_2. \tag{13}$$

The contribution of the zero angular harmonic is calculated as follows,

$$\sum_{\boldsymbol{p}} \frac{v^2}{2} f_2 = \frac{K}{m^*\nu}, \tag{14}$$

where $K = \nu \sum_{\boldsymbol{p}} (m^* v^2/2) f_2$ is the density of the excess kinetic energy of electrons. If the energy relaxation of electrons is faster than the energy diffusion, the excess energy K can be found from the balance between the energy gain from the high-frequency field $2(\mathrm{Re}\,\sigma)|\boldsymbol{E}_\parallel|^2$ and the energy dissipation K/τ_ε, where τ_ε is the energy relaxation time [54]. Thus, the energy balance gives $K = 2\tau_\varepsilon(\mathrm{Re}\,\sigma)|\boldsymbol{E}_\parallel|^2$. To calculate the contributions of the second angular harmonics, we multiply Eq. (7) by $v_x v_y$ or $v_x^2 - v_y^2$ and sum up the result over $\boldsymbol{p}$, which yields

$$\sum_{\boldsymbol{p}} v_x v_y f_2 = \frac{2\tau \mathrm{Re}\,\sigma}{m^*\nu} (E_x E_y^* + E_x^* E_y),$$

$$\sum_{\boldsymbol{p}} \frac{v_x^2 - v_y^2}{2} f_2 = \frac{2\tau \mathrm{Re}\,\sigma}{m^*\nu} (|E_x|^2 - |E_y|^2). \tag{15}$$

Finally, combining all the contributions to the photocurrent, we obtain

$$\boldsymbol{j} = \boldsymbol{j}^{(\mathrm{th})} + \boldsymbol{j}^{(\mathrm{pol})} + \boldsymbol{j}^{(\mathrm{ph})}, \tag{16}$$

where

$$\boldsymbol{j}^{(\mathrm{th})} = -2\frac{e\tau\tau_\varepsilon \,\mathrm{Re}\,\sigma}{m^*} \nabla S_0, \tag{17}$$

$$j_x^{(\mathrm{pol})} = -\frac{e\tau^2 \,\mathrm{Re}\,\sigma}{m^*} \left(\frac{\partial S_1}{\partial x} + \frac{\partial S_2}{\partial y} - \frac{1}{\omega\tau} \frac{\partial S_3}{\partial y} \right),$$

$$j_y^{(\mathrm{pol})} = -\frac{e\tau^2 \,\mathrm{Re}\,\sigma}{m^*} \left(\frac{\partial S_2}{\partial x} - \frac{\partial S_1}{\partial y} + \frac{1}{\omega\tau} \frac{\partial S_3}{\partial x} \right), \tag{18}$$

$$\boldsymbol{j}^{(\mathrm{ph})} = -2\frac{e\tau \,\mathrm{Re}\,\sigma}{m^*\omega} \mathrm{Im}(E_x \nabla E_x^* + E_y \nabla E_y^*), \tag{19}$$

$\mathrm{Re}\,\sigma = ne^2\tau/[m^*(1+\omega^2\tau^2)]$, $S_0 = |\boldsymbol{E}_\parallel|^2$, $S_1 = |E_x|^2 - |E_y|^2$, $S_2 = E_x E_y^* + E_x^* E_y$, and $S_3 = i(E_x E_y^* - E_x^* E_y)$. In the paraxial approximation for normally incident radiation, S_0, S_1, S_2, and S_3 correspond to the (non-normalized) Stokes parameters. The parameter S_0 describes the radiation intensity, S_1/S_0 and S_2/S_0 are the degrees of linear polarization in the (xy) axes and in the diagonal axes, respectively, and S_3/S_0 is the degree of circular polarization. All the above contributions to the dc current are proportional to the square of the electric field amplitude, i.e., the radiation intensity, and, therefore, belong to the class of photocurrents.

Besides the photothermoelectric current $\boldsymbol{j}^{(\mathrm{th})}$ originating from inhomogeneous heating and proportional to the gradient of the radiation intensity, the photocurrent contains the contributions $\boldsymbol{j}^{(\mathrm{pol})}$ and $\boldsymbol{j}^{(\mathrm{ph})}$. The first one, $\boldsymbol{j}^{(\mathrm{pol})}$ given by Eqs. (18), is determined by the gradients of the (non-normalized) polarization Stokes parameters S_j ($j = 1, 2, 3$). This photocurrent is induced by the electromagnetic field with spatially varying polarization, see Fig. 2, and emerges even if the field intensity is constant across the 2D gas plane. It is also induced by the field with a fixed polarization but nonuniform intensity, e.g., when the ratio S_j/S_0 is constant but S_0 depends on $\boldsymbol{r}$. In this particular case, the photocurrent $\boldsymbol{j}^{(\mathrm{pol})}$ can be seen as proportional to the in-plane gradient of the radiation intensity, similarly to the photothermoelectric contribution. However, its direction is determined by the field polarization and it can flow both along or perpendicularly to the intensity gradient. The polarization-sensitive photocurrent flowing perpendicularly to the intensity gradient is somewhat similar to the edge photogalvanic current in 2DEG [26,55].

The contribution $\boldsymbol{j}^{(\mathrm{ph})}$ given by Eq. (19) does not even require polarization gradients to emerge. For the field $\boldsymbol{E}(\boldsymbol{r}) = \boldsymbol{E}_0 e^{i\varphi(\boldsymbol{r})}$ with the constant amplitude and polarization, the photocurrent $\boldsymbol{j}^{(\mathrm{ph})}$ is proportional to the gradient of the phase $\varphi(\boldsymbol{r})$. An example of such a field $\boldsymbol{E}(\boldsymbol{r})$ is the plane electromagnetic wave obliquely incident on the 2D system. In this geometry, the phase varies linearly in 2D plane as $\varphi = \boldsymbol{q}_\parallel \cdot \boldsymbol{r}$, where $\boldsymbol{q}_\parallel$ is the in-plane component of the wave vector. The emerging photocurrent $\boldsymbol{j}^{(\mathrm{ph})} \propto \boldsymbol{q}_\parallel |\boldsymbol{E}_\parallel|^2$ is proportional to the in-plane wave vector $\boldsymbol{q}_\parallel$ and corresponds to the photon drag effect [41,43,45]. Thus, the phase-sensitive contribution $\boldsymbol{j}^{(\mathrm{ph})}$ given by Eq. (19) can be viewed as a generalization of the photon drag effect to the electromagnetic field with arbitrary varying phase.

All the photocurrent contributions discussed above are proportional to the cube of the electric charge e. It means that the photocurrents excited in n-type and p-type structures are directed oppositely while the flows of carriers, electrons or holes, are co-directed.

Equation (16) with the contributions (18) and (19) is the main result of our work. It describes the generation of dc current in 2DEG by arbitrary spatially inhomogeneous electromagnetic field. Below, we apply it to study the photocurrents induced by fields with polarization gradients and by beams of twisted light.

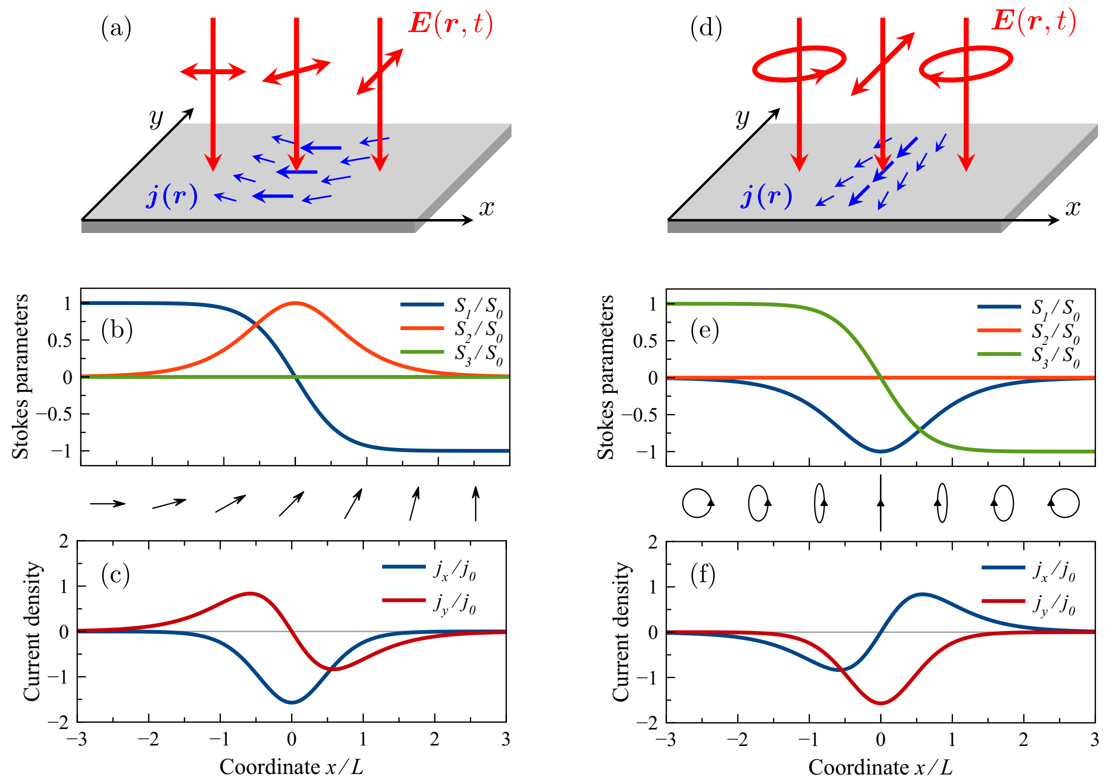

FIG. 2. The ac electromagnetic field $\boldsymbol{E}(\boldsymbol{r},t)$ with spatially inhomogeneous polarization induces direct photocurrents $\boldsymbol{j}(\boldsymbol{r})$ in the regions where the polarization varies. (a)–(c) Photocurrents induced by linearly polarized radiation whose polarization vector turns in the electron gas plane. (b) Spatial profiles of the Stokes parameters $S_j(x)/S_0$ of the incident radiation. The in-plane field polarizations are shown by black arrows. (c) Spatial distribution of the x and y components of the photocurrent density $\boldsymbol{j}(x)$. (d)–(f) Photocurrents induced by radiation with the polarization varying from left-handed to right-handed circular polarization. (e) Spatial profiles of the Stokes parameters $S_j(x)/S_0$ of the incident radiation. The field polarizations are shown by black arrows and ellipses. (f) Spatial distribution of the x and y components of the photocurrent density $\boldsymbol{j}(x)$ at $\omega\tau = 1$.

III. PHOTOCURRENTS INDUCED BY GRADIENTS OF FIELD POLARIZATION

Consider the photocurrents induced by electromagnetic fields with the constant in-plane amplitude $|\boldsymbol{E}_\parallel|$ in the 2DEG plane and the polarization varying along the x axis. Figures 2(a) and 2(d) show examples of such fields. In Fig. 2(a), the field $\boldsymbol{E}_\parallel$ is linearly polarized and the polarization rotates from $\boldsymbol{E}_\parallel \parallel x$ at large negative x to $\boldsymbol{E}_\parallel \parallel y$ at large positive x. In Fig. 2(d), the field polarization varies from the left-handed to the right-handed circular polarization through the linear polarization.

Figures 2(b) and 2(c) show the spatial dependence of the Stokes parameters and the spatial distribution of the emergent photocurrent density $\boldsymbol{j}(x)$ for the radiation sketched in Fig. 2(a). The polarization parameter S_1/S_0 varies from $+1$ at $x \to -\infty$ to -1 at $x \to +\infty$ whereas S_2/S_0 vanishes at $x \to \pm\infty$ and reaches its maximum value of 1 at $x = 0$. We take the spatial profile of the electric field amplitude in the form $E_x = E_0 \cos\Phi(x)$, $E_y = E_0 \sin\Phi(x)$, where $\Phi(x) = (\pi/4)[\tanh(x/L) + 1]$, which corresponds to the Stokes parameters $S_0 = E_0^2$, $S_1 = E_0^2 \cos 2\Phi(x)$, $S_2 = E_0^2 \sin 2\Phi(x)$, and $S_3 = 0$. As follows from Eqs. (17)–(19), the currents $\boldsymbol{j}^{(\mathrm{th})}$ and $\boldsymbol{j}^{(\mathrm{ph})}$ vanish for such a field, and the photoresponse is determined by the polarization-sensitive contribution $\boldsymbol{j}^{(\mathrm{pol})}$. The current $\boldsymbol{j}^{(\mathrm{pol})}$ emerges in the region where S_1 and S_2 vary, with $j_x^{(\mathrm{pol})} \propto \partial S_1/\partial x$ and $j_y^{(\mathrm{pol})} \propto \partial S_2/\partial x$. As a result, the photocurrent $\boldsymbol{j}$ has both components

$$j_x(x) = -\frac{\pi}{2}\frac{\cos[(\pi/2)\tanh(x/L)]}{\cosh^2(x/L)} j_0,$$
$$j_y(x) = -\frac{\pi}{2}\frac{\sin[(\pi/2)\tanh(x/L)]}{\cosh^2(x/L)} j_0, \tag{20}$$

where $j_0 = -ne^3\tau^3E_0^2/[m^{*2}L(1+\omega^2\tau^2)]$. The distributions $j_x(x)$ and $j_y(x)$ are plotted in Fig. 2(c). On average, the carriers (electrons with $e < 0$ or holes with $e > 0$) flow from the domain with $\boldsymbol{E}_\parallel \parallel x$ to the domain with $\boldsymbol{E}_\parallel \parallel y$.

Figures 2(e) and 2(f) show the spatial distributions of the Stokes parameters and the photocurrent density for the radiation with varying helicity as sketched in Fig. 2(d). Here, the profile of the electric field amplitude is taken in the form $E_x = iE_0 \sin\Phi(x)$, $E_y = E_0 \cos\Phi(x)$, where $\Phi(x) = (\pi/4)\tanh(x/L)$. The corresponding Stokes parameters have the form $S_0 = E_0^2$, $S_1 = -E_0^2 \cos 2\Phi(x)$, $S_2 = 0$, and $S_3 = -E_0^2 \sin 2\Phi(x)$. For this electromagnetic field, the photocurrent $\boldsymbol{j}$ is also solely determined by the polarization-sensitive contribution $\boldsymbol{j}^{(\mathrm{pol})}$ with the projections $j_x^{(\mathrm{pol})} \propto \partial S_1/\partial x$ and $j_y^{(\mathrm{pol})} \propto \partial S_3/\partial x$. Thus, the spatial distributions of the photocurrent components are given by the functions

$$j_x(x) = \frac{\pi}{2}\frac{\sin[(\pi/2)\tanh(x/L)]}{\cosh^2(x/L)}\, j_0,$$
$$j_y(x) = -\frac{\pi}{2}\frac{\cos[(\pi/2)\tanh(x/L)]}{\cosh^2(x/L)}\frac{j_0}{\omega\tau}, \tag{21}$$

which are plotted in Fig. 2(f).

Interestingly, the photocurrent between the domains with left-handed and right-handed circular polarizations flows along the boundary of the domains, as sketched in Fig. 2(d). The total boundary current

$$J_y = \int j_y(x)dx = -\frac{ne^3\tau^2[S_3(+\infty) - S_3(-\infty)]}{m^{*2}\omega(1+\omega^2\tau^2)} \tag{22}$$

does not depend on the domain boundary structure or the boundary width L and is determined by the difference of the Stokes parameter S_3 in the domains. Moreover, in the collisionless limit, i.e., at $\omega\tau \gg 1$, the current J_y is independent of the relaxation time τ. These features allow us to attribute the photocurrent J_y to the chiral edge current emerging between the photoinduced topological phases with the opposite Floquet-Chern numbers [49,50].

The photocurrent (22) is estimated as $J_y \approx 20\ \mu\text{A}$ for the carrier density $n = 5\times 10^{11}\ \text{cm}^{-2}$, the relaxation time $\tau = 1$ ps, the effective mass $m^* = 0.03m_0$, where m_0 is the free-electron mass, which correspond to bilayer graphene [26], $\omega\tau = 1$, and the electric field amplitude $E_\parallel = 0.25$ kV/cm corresponding to the terahertz radiation intensity $I = 1\ \text{kW/cm}^2$.

IV. PHOTOCURRENTS INDUCED BY TWISTED RADIATION

Now, we apply the developed theory to calculate the photoresponse of 2DEG to the twisted radiation, i.e., the electromagnetic waves carrying orbital angular momentum, Fig. 1. Such calculations can be conveniently done in the polar coordinate frame with the radial $\boldsymbol{e}_r = (\cos\varphi, \sin\varphi)$ and azimuthal $\boldsymbol{e}_\varphi = (-\sin\varphi, \cos\varphi)$ unit vectors, where φ is the polar angle counted from the x axis. In this frame, the photocurrents $\boldsymbol{j}^{(\text{th})}$, $\boldsymbol{j}^{(\text{pol})}$, and $\boldsymbol{j}^{(\text{ph})}$ are given by

$$\boldsymbol{j}^{(\text{th})} = -2\frac{e\tau\tau_\varepsilon \operatorname{Re}\sigma}{m^*}\nabla P_0, \tag{23}$$

$$j_r^{(\text{pol})} = -\frac{e\tau^2\operatorname{Re}\sigma}{m^*}\left(\frac{\partial P_1}{\partial r} + \frac{2P_1}{r} + \frac{1}{r}\frac{\partial P_2}{\partial\varphi} - \frac{1}{\omega\tau}\frac{1}{r}\frac{\partial P_3}{\partial\varphi}\right),$$
$$j_\varphi^{(\text{pol})} = \frac{e\tau^2\operatorname{Re}\sigma}{m^*}\left(\frac{1}{r}\frac{\partial P_1}{\partial\varphi} - \frac{\partial P_2}{\partial r} - \frac{2P_2}{r} - \frac{1}{\omega\tau}\frac{\partial P_3}{\partial r}\right), \tag{24}$$

$$\boldsymbol{j}^{(\text{ph})} = -2\frac{e\tau\operatorname{Re}\sigma}{m^*\omega}\left[\operatorname{Im}(E_r\nabla E_r^* + E_\varphi\nabla E_\varphi^*) + P_3\frac{\boldsymbol{e}_\varphi}{r}\right], \tag{25}$$

where $\nabla = \boldsymbol{e}_r\partial_r + (\boldsymbol{e}_\varphi/r)\partial_\varphi$, $P_0 = |E_r|^2 + |E_\varphi|^2 = S_0$, $P_1 = |E_r|^2 - |E_\varphi|^2$, $P_2 = E_rE_\varphi^* + E_r^*E_\varphi$, and $P_3 = i(E_rE_\varphi^* - E_r^*E_\varphi) = S_3$. In the paraxial approximation, P_0, P_1, P_2, and P_3 correspond to the Stokes parameters in the local coordinate frame $(\boldsymbol{e}_r, \boldsymbol{e}_\varphi)$. The presence of the terms in Eqs. (24) and (25) which do not contain derivatives is due to the fact that the directions of the $\boldsymbol{e}_r$ and $\boldsymbol{e}_\varphi$ vectors depend on φ.

As a commonly used example, we consider the class of the Bessel beams which are characterized by the integer index m of the projection of the total angular momentum onto the beam axis [4,5,16,56]. The electric field in the beam decomposed over the plane waves has the form

$$\boldsymbol{E}(\boldsymbol{r}, z) = E_0 e^{iq_z z}\sum_{\boldsymbol{q}_\parallel} a(\boldsymbol{q}_\parallel)\exp\left(i\boldsymbol{q}_\parallel\cdot\boldsymbol{r}\right)\boldsymbol{e}_{\boldsymbol{q}}, \tag{26}$$

where E_0 is the amplitude, $\boldsymbol{q} = (\boldsymbol{q}_\parallel, q_z)$ is the wave vector with the in-plane component $\boldsymbol{q}_\parallel$, $q = \omega n_\omega/c$, n_ω is the refractive index of the medium, $\boldsymbol{e}_{\boldsymbol{q}} \perp \boldsymbol{q}$ is the unit polarization vector of the plane wave, and $a(\boldsymbol{q}_\parallel)$ is the Fourier coefficient. The Bessel beams are formed from the plane waves with the wave vectors $\boldsymbol{q}$ lying on the surface of the cone with a certain angle θ_q and the axis parallel to z. Therefore, $q_z = q\cos\theta_q$ and $q_\parallel = q\sin\theta_q$ are fixed, and the integration in Eq. (26) is performed over the directions of the wave vector $\boldsymbol{q}_\parallel$.

The vector $\boldsymbol{e}_{\boldsymbol{q}}$ determines the polarization (spin momentum) of the plane waves constituting the Bessel beam. We take $\boldsymbol{e}_{\boldsymbol{q}}$ in the form

$$\boldsymbol{e}_{\boldsymbol{q}} = \alpha\,\boldsymbol{e}_{\theta q} + \beta\,\boldsymbol{e}_{\varphi q}, \tag{27}$$

where α and β are complex numbers, $|\alpha|^2 + |\beta|^2 = 1$, and $\boldsymbol{e}_{\theta q} = (\cos\theta_q\cos\varphi_q, \cos\theta_q\sin\varphi_q, -\sin\theta_q)$ and $\boldsymbol{e}_{\varphi q} = (-\sin\varphi_q, \cos\varphi_q, 0)$ are the unit vectors orthogonal to each other and to the wave vector $\boldsymbol{q}$. The cases of $\alpha = 1/\sqrt{2}$ and $\beta = \pm i/\sqrt{2}$, for example, correspond to the beams composed of the circularly polarized plane waves. The total angular momentum projection m of the twisted field is determined by the dependence of $a(\boldsymbol{q}_\parallel)$ on the polar angle φ_q of the in-plane wave vector $\boldsymbol{q}_\parallel$, which is taken in the form

$$a(\boldsymbol{q}_\parallel) = i^{-m-1}(2\pi/q_\parallel)\delta(q_\parallel - q\sin\theta_q)\exp(im\varphi_q). \tag{28}$$

By calculating the sum in Eq. (26) with $\boldsymbol{e}_{\boldsymbol{q}}$ and $a(\boldsymbol{q}_\parallel)$ given by Eqs. (27) and (28), respectively, one obtains the in-plane components of the electric field in the polar coordinate frame and in the paraxial approximation ($\theta_q \ll 1$) [4],

$$E_r(r,\varphi) = \frac{E_0}{2}e^{im\varphi}[o_+J_{m+1}(q_\parallel r) - o_-J_{m-1}(q_\parallel r)],$$
$$E_\varphi(r,\varphi) = \frac{E_0}{2i}e^{im\varphi}[o_+J_{m+1}(q_\parallel r) + o_-J_{m-1}(q_\parallel r)], \tag{29}$$

where $o_\pm = \alpha \pm i\beta$ and J_m is the Bessel function with the index m. In particular, $o_\pm = 1$ for the "radial" Bessel beam constructed from p-polarized plane waves ($\alpha = 1, \beta = 0$) and $o_\pm = \pm i$ for the "azimuthal" Bessel beam constructed from s-polarized waves ($\alpha = 0, \beta = 1$). For the Bessel beams constructed from circularly polarized plane waves, only one of the coefficients, either o_+ or o_-, is nonzero.

The straightforward calculation of the photocurrent components (23)–(25) with the electric field given by Eq. (29) yields $j_\varphi^{(\text{th})} = 0$,

$$j_r^{(\text{th})} = j_0\frac{\tau_\varepsilon}{\tau}\{J_{m+1}(J_m - J_{m+2}) - J_{m-1}(J_m - J_{m-2})$$
$$- [J_{m+1}(J_m - J_{m+2}) + J_{m-1}(J_m - J_{m-2})]\,p_3\}, \tag{30}$$

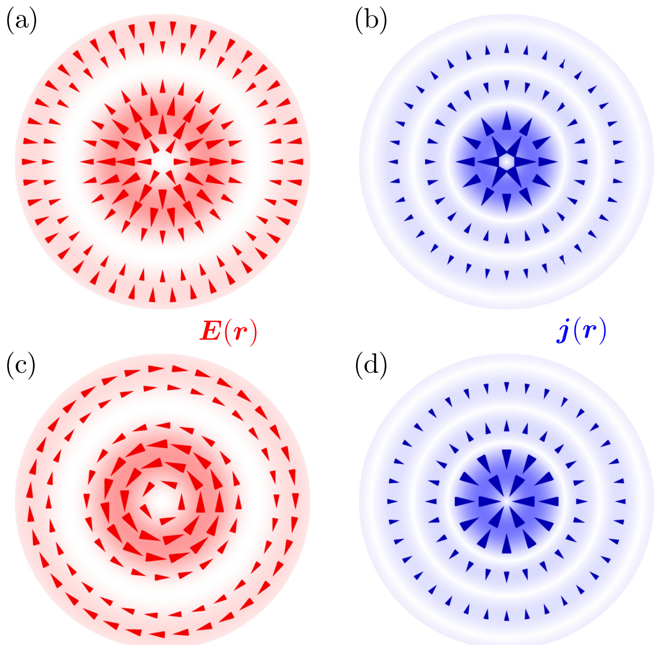

FIG. 3. Photocurrents induced by the radial and azimuthal Bessel beams with $m = 0$. (a) and (b) Distributions of the electric field vector $\boldsymbol{E}(\boldsymbol{r})$ and the photocurrent density $\boldsymbol{j}(\boldsymbol{r}) = \boldsymbol{j}^{(\mathrm{pol})} + \boldsymbol{j}^{(\mathrm{ph})}$ for the radial Bessel beam. (c) and (d) Distributions of the electric field vector $\boldsymbol{E}(\boldsymbol{r})$ and the photocurrent $\boldsymbol{j}(\boldsymbol{r})$ for the azimuthal Bessel beam. Red and blue backgrounds encode the radiation intensity and the magnitude of the photocurrent density, respectively.

$$
\begin{aligned}
j_r^{(\mathrm{pol})} + j_r^{(\mathrm{ph})} &= j_0 J_m (J_{m+1} - J_{m-1})\, p_1, \\
j_\varphi^{(\mathrm{pol})} + j_\varphi^{(\mathrm{ph})} &= j_0 J_m (J_{m+1} - J_{m-1}) \left(p_2 + \frac{p_3}{\omega\tau} \right) \\
&\quad - \frac{j_0}{\omega\tau} J_m (J_{m+1} + J_{m-1}),
\end{aligned} \tag{31}
$$

where

$$
j_0 = -\frac{n e^3 \tau^3 E_0^2 q_\parallel}{m^{*2}(1 + \omega^2\tau^2)}, \tag{32}
$$

$p_1 = |\alpha|^2 - |\beta|^2$, $p_2 = \alpha\beta^* + \alpha^*\beta$, and $p_3 = i(\alpha\beta^* - \alpha^*\beta)$ are the polarization parameters of the plane waves constituting the Bessel beam, and $J_m = J_m(q_\parallel r)$.

Now, we illustrate the photocurrents induced by Bessel beams with different polarizations and angular momentum projections. We focus on the polarization- and phase-sensitive photocurrents $\boldsymbol{j}^{(\mathrm{pol})} + \boldsymbol{j}^{(\mathrm{ph})}$. The photothermoelectric current $\boldsymbol{j}^{(\mathrm{th})}$ has only a radial component and is determined solely by the gradient of the radiation intensity. Note that, for the beams composed of circularly or elliptically polarized plane waves ($p_3 \neq 0$), the spatial distribution of the radiation intensity and, hence, the photothermoelectric current depend on the sign of circular polarization; see Eq. (30).

Figure 3 shows the spatial distributions of the ac electric field and the photocurrent density for the radial ($p_1 = 1$) and azimuthal ($p_1 = -1$) Bessel beams with the total angular momentum projection $m = 0$. In these particular cases, the electric field in the beams has only radial or azimuthal component, and the field distribution is rotationally invariant, Figs. 3(a) and 3(c). For the both beams, the photocurrent has only a radial component, Figs. 3(b) and 3(d). The current density is nonmonotonic and oscillates with the distance from the beam center; these oscillations originate from the radial distribution of the electric field. While the local current magnitude is the same for the radial and azimuthal Bessel beams, the current directions are opposite and controlled by the polarization of plane waves constituting the beams. Note that the photothermoelectric effect also produces a radial electric current. This contribution, however, is independent of the linear polarization and, therefore, can be experimentally separated.

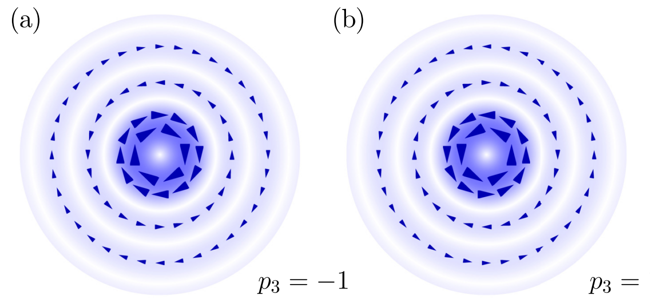

FIG. 4. Spatial distributions of the photocurrent density $\boldsymbol{j}(\boldsymbol{r}) = \boldsymbol{j}^{(\mathrm{pol})} + \boldsymbol{j}^{(\mathrm{ph})}$ for the Bessel beams with $m = 0$ composed of (a) left-handed ($p_3 = -1$) and (b) right-handed ($p_3 = 1$) circularly polarized plane waves. The current $\boldsymbol{j}$ forms vortices with the winding direction determined by the radiation helicity.

Whereas the photocurrents induced by the radial and azimuthal Bessel beams with $m = 0$ flow radially, the photocurrents induced by the beams composed of circularly polarized plane waves ($p_3 = \pm 1$) have polarization-sensitive azimuthal components. This is shown in Fig. 4 for the Bessel beams with $m = 0$. In these cases, the photocurrents form vortices (here, the sets of concentric current loops with alternating directions) with the winding direction determined by the radiation helicity.

For the Bessel beams with $m \neq 0$, the spatial distributions of the ac field amplitude and the photocurrent density get more complex with the radial and azimuthal components intermixed. Figures 5(a) and 5(c) show the snapshots of the electric field distributions in the radial ($p_1 = 1$) Bessel beams with $m = \pm 2$ at a certain time t_0. The field distributions at any time t are obtained by the rotation of the given distributions by the angle $\varphi = \omega(t - t_0)/m$, as indicated by bent red arrows. Far from the beam center, the field is linearly polarized along the radius, whereas at the beam core the polarization is elliptical. Figures 5(b) and 5(d) show the distributions of the photocurrent density in the beams. The photocurrents contain both radial and azimuthal components. The direction of the azimuthal component is controlled by the sign of m and, hence, it is opposite in Figs. 5(b) and 5(d).

Figure 6 shows the spatial distributions of the photocurrent density for the Bessel beams with $m = \pm 1$ composed of the left-handed ($p_3 = -1$) and the right-handed ($p_3 = 1$) circularly polarized plane waves. Similarly to the case of $m = 0$ (Fig. 4), the photocurrents have polarization-sensitive

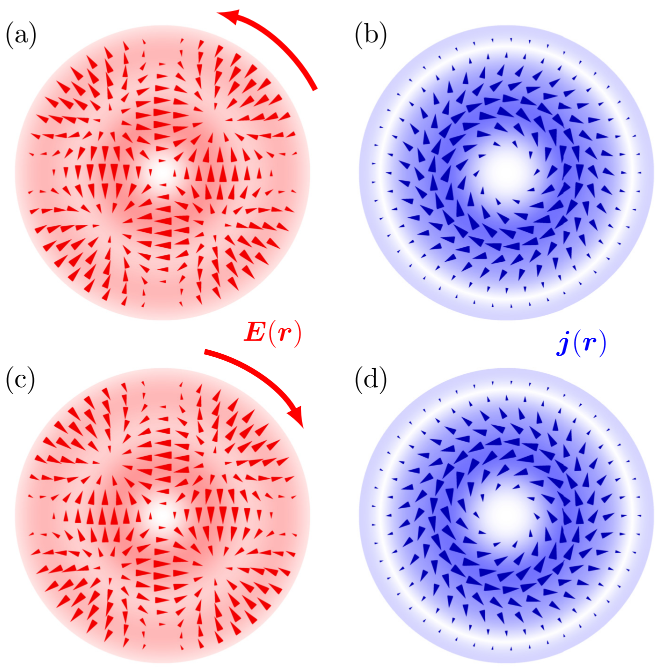

FIG. 5. Photocurrents induced by the radial Bessel beams with $m = \pm 2$. (a) and (c) Snapshots of electric field distributions in the cross sections of the beams. (b) and (d) Distributions of the photocurrent density $\boldsymbol{j}(\boldsymbol{r}) = \boldsymbol{j}^{(\text{pol})} + \boldsymbol{j}^{(\text{ph})}$ for the corresponding Bessel beams.

azimuthal components and form vortices. The current distribution in the beam cross section is determined by both the total angular momentum projection m and the radiation

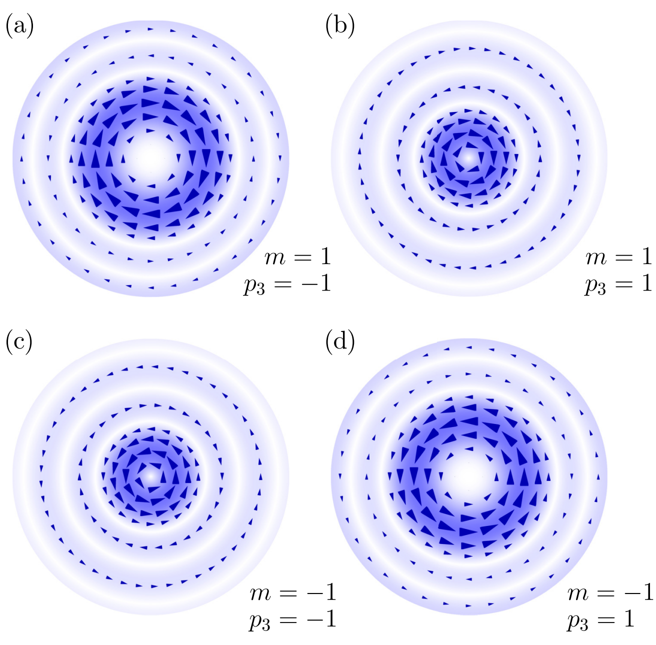

FIG. 6. Spatial distributions of the photocurrent density $\boldsymbol{j}(\boldsymbol{r}) = \boldsymbol{j}^{(\text{pol})} + \boldsymbol{j}^{(\text{ph})}$ for the Bessel beams with $m = \pm 1$ composed of left-handed ($p_3 = -1$) and right-handed ($p_3 = 1$) circularly polarized plane waves. (a) $m = 1,\ \ p_3 = -1$; (b) $m = 1,\ \ p_3 = 1$; (c) $m = -1,\ \ p_3 = -1$; and (d) $m = -1,\ \ p_3 = 1$.

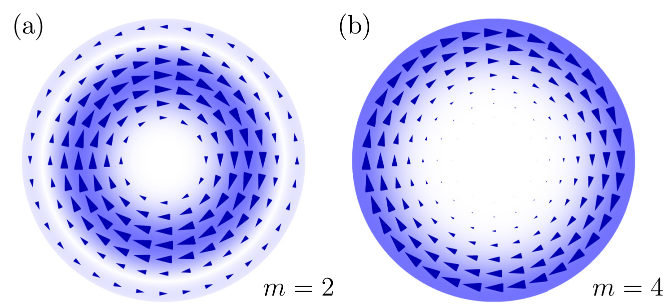

FIG. 7. Spatial distributions of the photocurrent density $\boldsymbol{j}(\boldsymbol{r}) = \boldsymbol{j}^{(\text{pol})} + \boldsymbol{j}^{(\text{ph})}$ for the Bessel beams with (a) $m = 2$ and (b) $m = 4$ composed of left-handed circularly polarized plane waves.

helicity. Reversing the sign of both m and p_3 mirrors the distributions; cf. Figs. 6(a) and 6(d) or Figs. 6(b) and 6(c).

Completing the discussion of photocurrent distributions, we note that the radius of the first circle in the Bessel beam increases almost linearly with the absolute value of the orbital angular momentum projection $|l| = |m - p_3|$ [4]. So does the radius of the first current loop. This is shown in Fig. 7, where the spatial distributions of the current density are plotted for the Bessel beams with $m = 2$ and $m = 4$.

Radial photocurrents j_r lead to a redistribution of electric charge in the 2DEG plane and, hence, to the (nonuniform) electrostatic potential $U(r)$, which, in turn, results in the radial drift current $j_r^{(\text{drift})} = -\sigma_0\, dU/dr$, where $\sigma_0 = ne^2\tau/m^*$ is the static conductivity. In the open circuit configuration, the total radial current in the steady-state regime vanishes, $j_r + j_r^{(\text{drift})} = 0$, which yields

$$U(r) - U(0) = \frac{1}{\sigma_0}\int_0^r j_r(r')dr'. \tag{33}$$

Therefore, for the photocurrents induced by the Bessel beams, Eqs. (30) and (31), we obtain

$$\begin{aligned} U(r) - U(0) = {} & U_0\big[\delta_{m,0} - J_m^2(q_\parallel r)\big]p_1 \\ & + U_0\frac{\tau_\varepsilon}{\tau}\sum_{s=\pm 1}\big[J_{m+s}^2(q_\parallel r) - \delta_{m+s,0}\big](1 - sp_3), \end{aligned} \tag{34}$$

where

$$U_0 = -\frac{e\tau^2 E_0^2}{m^*(1 + \omega^2\tau^2)}, \tag{35}$$

and J_m is the Bessel function. Interestingly, $U(\infty) - U(0)$ does not vanish for the beams with $m = 0, \pm 1$ only. This voltage is determined solely by the photocurrent $j_r^{(\text{pol})} + j_r^{(\text{ph})}$ for the beams with $m = 0$ and by the photothermoelectric current $j_r^{(\text{th})}$ for the beams with $m = \pm 1$. The photovoltage U_0 is of the order of 1 mV for the terahertz beams with the intensity 1 kW/cm^2 and the structure parameters listed in the end of Sec. III.

Azimuthal photocurrents j_φ do not produce voltage drops in homogeneous 2D systems [57]. What they produce is a static magnetic field $\boldsymbol{B}_{\text{photo}}$, which points along the 2DEG plane normal at $z = 0$. At the center of the beam, the field can be readily calculated from the Biot-Savart law

$$B_{\text{photo}} = \frac{2\pi}{c}\int_0^{+\infty} \frac{j_\varphi(r)}{r} dr. \tag{36}$$

For the azimuthal photocurrent given by Eq. (31), we obtain

$$B_{\text{photo}} = \frac{8j_0}{c(4m^2-1)}\left(p_2 + \frac{p_3}{\omega\tau} + \frac{2m}{\omega\tau}\right), \tag{37}$$

where $j_0 = -ne^3\tau^3E_0^2q_\parallel/[m^{*2}(1+\omega^2\tau^2)]$. The first two contributions in Eq. (37) depend on the polarization parameters p_2 and p_3 of the plane waves constituting the beam. The third contribution is polarization-independent but reverses its sign upon changing the sign of m. At large values of the total angular momentum projection, $|m| \gg 1$, the polarization-independent contribution dominates and the magnetic field assumes the dependence $B_{\text{photo}} \propto 1/m$. Estimation of the current density for $q_\parallel/q = 0.1$ and the radiation intensity 1 kW/cm^2 yields $j_0 \approx 30\,\mu$A/cm. The corresponding magnetic field B_{photo} is of the order of nT. Such fields can be detected, e.g., by SQUIDs [58] or optical sensors based on color centers in silicon carbide or diamond [59]. The emergence of a static magnetization controlled by the angular momentum of the beam can be considered as the inverse Faraday effect [60] of twisted light.

V. CONCLUSIONS

In summary, we have studied the generation of direct electric currents in two-dimensional electron systems driven by electromagnetic radiation with structured intensity, polarization, and phase. The theory of such a nonlinear and nonlocal response is developed within the kinetic approach for the intraband electron transport, which, for semiconductor structures, corresponds to the radiation of radio-frequency and terahertz spectral ranges. The derived analytical expressions for the photocurrent contributions are general and can be applied to the radiation with an arbitrary spatial profile. In particular, the photocurrents are induced by the radiation with a uniform intensity but spatially varying polarization in the 2D plane, e.g., at the boundary between the domains excited by radiation with different polarization states. The total current emerging at the boundary of the domains excited by circularly polarized radiation with the opposite helicity flow along the boundary and does not depend on the boundary structure or the electron gas mobility in the high-frequency limit. Its value for bilayer graphene is estimated as 20 μA for terahertz radiation with the intensity 1 kW/cm^2.

The photocurrents induced by the Bessel beams carrying orbital angular momentum have both the radial and azimuthal (vortex-like) components controlled by the beam polarization and angular momentum. In the experiments conducted in the open-circuit configuration, the radial photocurrents lead to a charge redistribution in the sample and, hence, to a nonuniform electrostatic potential and oppositely directed drift currents. The amplitude of the resulting voltage sensitive to the beam polarization and angular momentum is of the order of 1 mV for the terahertz beams with the intensity 1 kW/cm^2. The azimuthal photocurrents, in turn, do not produce voltage drops in homogeneous 2D systems; however, they create a tiny static magnetic field directed perpendicular to the sample. We have calculated the photoinduced electrostatic potential and the photoinduced magnetic field and analyzed their dependence on the beam parameters. The analysis suggests that the measurement of the photoresponse provides a useful experimental tool to determine the parameters of structured radiation, such as the photon spin and orbital angular momentum.

ACKNOWLEDGMENT

This work was supported by the Russian Science Foundation (Project No. 22-12-00211).

[1] A. Forbes, M. de Oliveira, and M. R. Dennis, Structured light, Nat. Photonics **15**, 253 (2021).

[2] L. Allen, M. J. Padgett, and M. Babiker, IV. The orbital angular momentum of light, Prog. Opt. **39**, 291 (1999).

[3] G. Molina-Terriza, J. P. Torres, and L. Torner, Twisted photons, Nat. Phys. **3**, 305 (2007).

[4] B. A. Knyazev and V. G. Serbo, Beams of photons with nonzero orbital angular momentum projection: New results, Phys. Usp. **61**, 449 (2018).

[5] C. Maurer, A. Jesacher, S. Fürhapter, S. Bernet, and M. Ritsch-Marte, Tailoring of arbitrary optical vector beams, New J. Phys. **9**, 78 (2007).

[6] X. Wei, C. Liu, L. Niu, Z. Zhang, K. Wang, Z. Yang, and J. Liu, Generation of arbitrary order Bessel beams via 3D printed axicons at the terahertz frequency range, Appl. Opt. **54**, 10641 (2015).

[7] Y. Y. Choporova, B. A. Knyazev, G. N. Kulipanov, V. S. Pavelyev, M. A. Scheglov, N. A. Vinokurov, B. O. Volodkin, and V. N. Zhabin, High-power Bessel beams with orbital angular momentum in the terahertz range, Phys. Rev. A **96**, 023846 (2017).

[8] Z. Zhang, Q. Xingdu, M. Bikashkali, L. Kevin, S. Jingbo, W. Tianwei, L. Wenjing, A. Ritesh, J. J. Miquel, L. Stefano, L. N. M., and F. Liang, Tunable topological charge vortex microlaser, Science **368**, 760 (2020).

[9] A. Ashkin, History of optical trapping and manipulation of small-neutral particle, atoms, and molecules, IEEE J. Sel. Top. Quantum Electron. **6**, 841 (2000).

[10] D. L. Andrews, *Structured Light and Its Applications: An Introduction to Phase-Structured Beams and Nanoscale Optical Forces* (Academic Press, Cambridge, 2011).

[11] O. M. Maragò, P. H. Jones, P. G. Gucciardi, G. Volpe, and A. C. Ferrari, Optical trapping and manipulation of nanostructures, Nat. Nanotechnol. **8**, 807 (2013).

[12] A. S. Urban, S. Carretero-Palacios, A. A. Lutich, T. Lohmüller, J. Feldmann, and F. Jäckel, Optical trapping and manipulation of plasmonic nanoparticles: Fundamentals, applications, and perspectives, Nanoscale **6**, 4458 (2014).

[13] V. N. Mantsevich and S. A. Tarasenko, Fluid photonic crystal from colloidal quantum dots, Phys. Rev. A **96**, 033855 (2017).

[14] Y. Yang, Y. Ren, M. Chen, Y. Arita, and C. Rosales-Guzmán, Optical trapping with structured light: A review, Adv. Photonics **3**, 034001 (2021).

[15] Z. Ji, W. Liu, S. Krylyuk, X. Fan, Z. Zhang, A. Pan, L. Feng, A. Davydov, and R. Agarwal, Photocurrent detection of the orbital angular momentum of light, Science **368**, 763 (2020).

[16] S. Sederberg, F. Kong, F. Hufnagel, C. Zhang, E. Karimi, and P. B. Corkum, Vectorized optoelectronic control and metrology in a semiconductor, Nat. Photon. **14**, 680 (2020).

[17] J. Lai, J. Ma, Z. Fan, X. Song, P. Yu, Z. Liu, P. Zhang, Y. Shi, J. Cheng, and D. Sun, Direct light orbital angular momentum detection in mid-infrared based on the type-II Weyl semimetal $TaIrTe_4$, Adv. Mater. **34**, 2201229 (2022).

[18] U. Bhattacharya, S. Chaudhary, T. Grass, A. S. Johnson, S. Wall, and M. Lewenstein, Fermionic Chern insulator from twisted light with linear polarization, Phys. Rev. B **105**, L081406 (2022).

[19] F. Meier and B. P. Zakharchenya (eds.), *Optical Orientation* (North Holland, Amsterdam, 1984).

[20] S. Hubmann, G. V. Budkin, M. Otteneder, D. But, D. Sacré, I. Yahniuk, K. Diendorfer, V. V. Bel'kov, D. A. Kozlov, N. N. Mikhailov, S. A. Dvoretsky, V. S. Varavin, V. G. Remesnik, S. A. Tarasenko, W. Knap, and S. D. Ganichev, Symmetry breaking and circular photogalvanic effect in epitaxial $Cd_xHg_{1-x}Te$ films, Phys. Rev. Mater. **4**, 043607 (2020).

[21] B. I. Sturman and V. M. Fridkin, *The Photovoltaic and Photorefractive Effects in Noncentrosymmetric Materials* (Gordon and Breach Science Publishers, Philadelphia, 1992).

[22] E. L. Ivchenko, *Optical Spectroscopy of Semiconductor Nanostructures* (Alpha Science, Oxford, 2005).

[23] J. E. Sipe and A. I. Shkrebtii, Second-order optical response in semiconductors, Phys. Rev. B **61**, 5337 (2000).

[24] S. A. Tarasenko, Direct current driven by ac electric field in quantum wells, Phys. Rev. B **83**, 035313 (2011).

[25] M. V. Durnev and S. A. Tarasenko, High-frequency nonlinear transport and photogalvanic effects in 2D topological insulators, Ann. Phys. **531**, 1800418 (2019).

[26] S. Candussio, M. V. Durnev, S. A. Tarasenko, J. Yin, J. Keil, Y. Yang, S.-K. Son, A. Mishchenko, H. Plank, V. V. Bel'kov, S. Slizovskiy, V. Fal'ko, and S. D. Ganichev, Edge photocurrent driven by terahertz electric field in bilayer graphene, Phys. Rev. B **102**, 045406 (2020).

[27] M. V. Durnev and S. A. Tarasenko, Edge photogalvanic effect caused by optical alignment of carrier momenta in two-dimensional Dirac materials, Phys. Rev. B **103**, 165411 (2021).

[28] J. F. Steiner, A. V. Andreev, and M. Breitkreiz, Surface photogalvanic effect in Weyl semimetals, Phys. Rev. Res. **4**, 023021 (2022).

[29] N. V. Leppenen and L. E. Golub, Linear photogalvanic effect in surface states of topological insulators, Phys. Rev. B **107**, L161403 (2023).

[30] A. V. Parafilo, M. V. Boev, V. M. Kovalev, and I. G. Savenko, Photogalvanic transport in fluctuating Ising superconductors, Phys. Rev. B **106**, 144502 (2022).

[31] G. F. Quinteiro and J. Berakdar, Electric currents induced by twisted light in quantum rings, Opt. Express **17**, 20465 (2009).

[32] J. Wätzel and J. Berakdar, Centrifugal photovoltaic and photogalvanic effects driven by structured light, Sci. Rep. **6**, 21475 (2016).

[33] J. Wätzel, E. Y. Sherman, and J. Berakdar, Nanostructures in structured light: Photoinduced spin and orbital electron dynamics, Phys. Rev. B **101**, 235304 (2020).

[34] G. F. Quinteiro and P. I. Tamborenea, Twisted-light-induced optical transitions in semiconductors: Free-carrier quantum kinetics, Phys. Rev. B **82**, 125207 (2010).

[35] A. M. Danishevskii, A. A. Kastalskii, S. M. Ryvkin, and I. D. Yaroshetskii, Dragging of free carriers by photons in direct interband transitions in semiconductors, Sov. Phys. JETP **31**, 292 (1970).

[36] A. F. Gibson, M. F. Kimmitt, and A. C. Walker, Photon drag in germanium, Appl. Phys. Lett. **17**, 75 (1970).

[37] V. I. Perel' and Ya. M. Pinskii, Constant current in conducting media due to a high-frequency electron electromagnetic field, Sov. Phys. Solid State **15**, 688 (1973).

[38] S. Luryi, Photon-Drag Effect in Intersubband Absorption by a Two-Dimensional Electron Gas, Phys. Rev. Lett. **58**, 2263 (1987).

[39] V. A. Shalygin, H. Diehl, C. Hoffmann, S. N. Danilov, T. Herrle, S. A. Tarasenko, D. Schuh, C. Gerl, W. Wegscheider, W. Prettl, and S. D. Ganichev, Spin photocurrents and the circular photon drag effect in (110)-grown quantum well structures, JETP Lett. **84**, 570 (2007).

[40] T. Hatano, T. Ishihara, S. G. Tikhodeev, and N. A. Gippius, Transverse Photovoltage Induced by Circularly Polarized Light, Phys. Rev. Lett. **103**, 103906 (2009).

[41] J. Karch, P. Olbrich, M. Schmalzbauer, C. Zoth, C. Brinsteiner, M. Fehrenbacher, U. Wurstbauer, M. M. Glazov, S. A. Tarasenko, E. L. Ivchenko, D. Weiss, J. Eroms, R. Yakimova, S. Lara-Avila, S. Kubatkin, and S. D. Ganichev, Dynamic Hall Effect Driven by Circularly Polarized Light in a Graphene Layer, Phys. Rev. Lett. **105**, 227402 (2010).

[42] M. V. Entin, L. I. Magarill, and D. L. Shepelyansky, Theory of resonant photon drag in monolayer graphene, Phys. Rev. B **81**, 165441 (2010).

[43] S. Stachel, G. V. Budkin, U. Hagner, V. V. Bel'kov, M. M. Glazov, S. A. Tarasenko, S. K. Clowes, T. Ashley, A. M. Gilbertson, and S. D. Ganichev, Cyclotron-resonance-assisted photon drag effect in InSb/InAlSb quantum wells excited by terahertz radiation, Phys. Rev. B **89**, 115435 (2014).

[44] P. A. Obraztsov, N. Kanda, K. Konishi, M. Kuwata-Gonokami, S. V. Garnov, A. N. Obraztsov, and Y. P. Svirko, Photon-drag-induced terahertz emission from graphene, Phys. Rev. B **90**, 241416(R) (2014).

[45] M. Glazov and S. Ganichev, High frequency electric field induced nonlinear effects in graphene, Phys. Rep. **535**, 101 (2014).

[46] H. Plank, L. E. Golub, S. Bauer, V. V. Bel'kov, T. Herrmann, P. Olbrich, M. Eschbach, L. Plucinski, C. M. Schneider, J. Kampmeier, M. Lanius, G. Mussler, D. Grützmacher, and S. D. Ganichev, Photon drag effect in $(Bi_{1-x}Sb_x)_2Te_3$ three-dimensional topological insulators, Phys. Rev. B **93**, 125434 (2016).

[47] G. M. Mikheev, A. S. Saushin, V. M. Styapshin, and Y. P. Svirko, Interplay of the photon drag and the surface photogalvanic effects in the metal-semiconductor nanocomposite, Sci. Rep. **8**, 8644 (2018).

[48] L.-k. Shi, D. Zhang, K. Chang, and J. C. W. Song, Geometric Photon-Drag Effect and Nonlinear Shift Current in Centrosymmetric Crystals, Phys. Rev. Lett. **126**, 197402 (2021).
[49] T. Kitagawa, T. Oka, A. Brataas, L. Fu, and E. Demler, Transport properties of nonequilibrium systems under the application of light: Photoinduced quantum Hall insulators without Landau levels, Phys. Rev. B **84**, 235108 (2011).
[50] N. H. Lindner, G. Refael, and V. Galitski, Floquet topological insulator in semiconductor quantum wells, Nat. Phys. **7**, 490 (2011).
[51] J. Lindhard, On the properties of a gas of charged particles, Kgl. Danske Videnskab. Selskab Mat.-Fys. Medd. **28**, 1 (1954).
[52] G. Giuliani and G. Vignale, *Quantum Theory of the Electron Liquid* (Cambridge University Press, Cambridge, 2005).
[53] See paragraph after Eq. (9) for details.
[54] To describe the energy relaxation of electrons one needs to go beyond the collision integral (4).
[55] M. V. Durnev and S. A. Tarasenko, Edge currents induced by ac electric field in two-dimensional Dirac structures, Appl. Sci. **13**, 4080 (2023).
[56] A. V. Nesterov and V. G. Niziev, Laser beams with axially symmetric polarization, J. Phys. D: Appl. Phys. **33**, 1817 (2000).
[57] In samples with special geometry, like split rings, azimuthal photocurrents can also be detected as voltage drops.
[58] K. C. Nowack, E. M. Spanton, M. Baenninger, M. König, J. R. Kirtley, B. Kalisky, C. Ames, P. Leubner, C. Brüne, H. Buhmann, L. W. Molenkamp, D. Goldhaber-Gordon, and K. A. Moler, Imaging currents in HgTe quantum wells in the quantum spin Hall regime, Nat. Mater. **12**, 787 (2013).
[59] D. Simin, V. A. Soltamov, A. V. Poshakinskiy, A. N. Anisimov, R. A. Babunts, D. O. Tolmachev, E. N. Mokhov, M. Trupke, S. A. Tarasenko, A. Sperlich, P. G. Baranov, V. Dyakonov, and G. V. Astakhov, All-Optical dc Nanotesla Magnetometry Using Silicon Vacancy Fine Structure in Isotopically Purified Silicon Carbide, Phys. Rev. X **6**, 031014 (2016).
[60] M. V. Durnev, Faraday and Kerr rotation due to photoinduced orbital magnetization in two-dimensional electron gas, arXiv:2306.08509.